NDT&E International 122 (2021) 102472

Contents lists available at ScienceDirect

NDT and E International

journal homepage: www.elsevier.com/locate/ndteint

Damage quantification in an aluminium-CFRP composite structure using guided wave wavenumber mapping: Comparison of instantaneous and local wavenumber analyses

Yevgeniya Lugovtsova [a,*], Jannis Bulling [a], Olivier Mesnil [b], Jens Prager [a], Dirk Gohlke [a], Christian Boller [c]

[a] Bundesanstalt für Materialforschung und -prüfung, Acoustic and Electromagnetic Methods Division, Unter Den Eichen 87, 12205, Berlin, Germany
[b] Université Paris-Saclay, CEA, List, France
[c] Saarland University, Chair of NDT and Quality Assurance (LZfPQ), Am Markt, Zeile 4, 6612, Saarbrücken, Germany

ARTICLE INFO

Keywords:
Ultrasonic guided waves
Instantaneous wavenumber analysis
Local wavenumber analysis
Signal processing

ABSTRACT

Composite-overwrapped pressure vessels (COPV) are increasingly used in the transportation industry due to their high strength to mass ratio. Throughout the years, various designs were developed and found their applications. Currently, there are five designs, which can be subdivided into two main categories - with a load-sharing metal liner and with a non-load-sharing plastic liner. The main damage mechanism defining the lifetime of the first type is fatigue of the metal liner, whereas for the second type it is fatigue of the composite overwrap. Nevertheless, one damage type which may drastically reduce the lifetime of COPV is impact-induced damage. Therefore, this barely visible damage needs to be assessed in a non-destructive way to decide whether the pressure vessel can be further used or has to be put out of service. One of the possible methods is based on ultrasonic waves. In this contribution, both conventional ultrasonic testing (UT) by high-frequency bulk waves and wavenumber mapping by low frequency guided waves are used to evaluate impact damage. Wavenumber mapping techniques are first benchmarked on a simulated aluminium panel then applied to experimental measurements acquired on a delaminated aluminium-CFRP composite plate which corresponds to a structure of COPV with a load-sharing metal liner. The analysis of experimental data obtained from measurements of guided waves propagating in an aluminium-CFRP composite plate with impact-induced damage is performed. All approaches show similar performance in terms of quantification of damage size and depths while being applied to numerical data. The approaches used on the experimental data deliver an accurate estimate of the in-plane size of the large delamination at the aluminium-CFRP interface but only a rough estimate of its depth. Moreover, none of the wavenumber mapping techniques used in the study can quantify every delamination between CFRP plies caused by the impact, which is the case for conventional UT. This may be solved by using higher frequencies (shorter wavelengths) or more advanced signal processing techniques. All in all, it can be concluded that imaging of complex impact damage in fibre-reinforced composites based on wavenumber mapping is not straightforward and stays a challenging task.

1. Introduction

The growing use of composite materials in aerospace, automotive and other applications is associated with weight reduction and improved structural performance [1–3]. However, the risk of barely visible impact damages or manufacturing damages exists which may be critical for the safe use of the component. There is, therefore, a need for techniques that can detect and characterise damage non-destructively. One of the promising methods is based on the propagation and analysis of ultrasonic guided waves. The multimodal nature and dispersive behaviour of these waves allow for detection and characterisation of various damage types, however, make the analysis of signals difficult [4–10]. For easier interpretation of the guided wave signals and extraction of the necessary information about the damage, advanced signal processing techniques have been proposed [11–19]. One of them is the wavenumber mapping which consists of creating a cartography of the wavenumber of a

* Corresponding author.
E-mail address: yevgeniya.lugovtsova@bam.de (Y. Lugovtsova).

https://doi.org/10.1016/j.ndteint.2021.102472
Received 29 June 2020; Received in revised form 7 April 2021; Accepted 12 May 2021
Available online 29 May 2021

propagating mode over an inspected area. The mode is typically excited using a piezoceramic transducer and a wavefield is measured with a scanning laser Doppler vibrometer, since a dense acquisition of data is required for the successful analysis. This technique allows both the quantification of the location, in-plane size of damage, and to some extent its depth, *i.e.*, corrosion in metals [16] or delamination in composite laminates [17,19–21].

Two local wavenumber techniques were proposed simultaneously by Flynn et al. [16] and Rogge et al. [17] allowing the size and depth of corrosion in metals and impact damage in composites, respectively, to be evaluated. Even though, both techniques are referred to as *local wavenumber* analysis, they retrieve the resulting wavenumber estimate in two different ways. Both techniques have similarity in how the wavefield is pre-processed using the three-dimensional fast Fourier transform (3DFFT) to separate the modes and different band-pass filters to remove undesirable modes leaving one mode of interest only. The filtered data is then transformed back to time domain utilising the inverse 3DFFT. The difference comes from the way how the filtered data is treated afterwards to retrieve the local wavenumber maps. Flynn et al. [16] decreases the dimensionality of the data by three-dimensional enveloping and summing across time to retrieve spatially-distributed wavenumber maps. The resulting local wavenumber is estimated by simply taking wavenumbers with the highest magnitudes for every spatial point. In contrast, Rogge et al. [17] multiply the data by a spatial window of a defined size and estimate wavenumbers locally within this window at the excitation frequency. The resulting wavenumber map consists of the dominant wavenumbers which are retrieved through the weighted-sum of the windowed wavenumber spectra. Later, Mesnil et al. [19] developed another technique called *instantaneous wavenumber* mapping and compared it to the local wavenumber technique introduced by Rogge et al. [17]. The pre-processing of the wavefield was done in a similar way as in Refs. [16,17], so that the mode of interest was isolated prior to the wavenumber mapping. The mapping itself is based on retrieving the phase of the signals using the Hilbert transform. An unwrapping step in each direction is necessary to retrieve a continuous phase, which is then derived so that the wavenumber vector can be calculated. The instantaneous wavenumber (IW) is the magnitude of the resulting wavenumber vector at a time instant. The authors also simplified the wavenumber mapping by introducing the concept of a single frequency wavefield analysis, which allows straightforward correlation of wavenumbers with the effective thicknesses and thus the damage depth. Parallelly, Juarez et al. [20] used the excitation frequency only to perform the local wavenumber mapping as of Rogge et al. [17] showing that it can be done in a more efficient way.

The present contribution complements the research conducted by Lugovtsova et al. [22], in which the impact damage in an aluminium-CFRP composite plate was successfully quantified using the IW mapping technique of [19]. Moreover, this contribution extends the work of [19], in which the analysis was performed for an idealized single delamination (a Teflon insert) to a real multi-layer delamination damage, introduced by a low-velocity impact. To the authors' knowledge, only two works of Rogge and Leckey [17], and Juarez and Leckey [20] investigated a realistic multi-layer delamination using wavenumber mapping. In their investigations the analysis was done using only the local wavenumber analysis based on multiple excitation frequencies. Therefore, in the current paper, a comparative analysis of the instantaneous and local wavenumber techniques is performed. It is first conducted on simulated data, followed by the evaluation based on experimental data. The local wavenumber mapping is performed using two types of windows on a numerical example of a damaged aluminium plate computed using CIVA [23,24]. The results are compared to the IW mapping technique and discussed based on their accuracy and computational performance. Then, the wavenumber mapping is applied to a delaminated aluminium-CFRP composite plate which corresponds to the structure of composite-overwrapped pressure vessels used for storing gases in aerospace and automotive industries. The analysis of experimental data obtained from the measurements of guided waves propagating in the composite plate with impact-induced damage is performed. Two cases are considered – one for the measurements performed on the Al-side and one from the CFRP-side of the composite plate. The output of the imaging is a three-dimensional representation of the delamination induced by the impact. The damage map obtained from the guided wave-based analysis is compared with the results from conventional ultrasonic testing.

This paper is organised as follows. In Section 2, the detailed description of the wavenumber techniques is given along with their application to a numerical data being the wavefield of the damaged aluminium plate. The workflows for data pre-processing and quantification of damage size and depth are introduced. In Section 3, the experimental set-up is described, followed by wavenumber mapping and damage quantification in the aluminium-CFRP composite plate. The results are then compared to the ones from the conventional ultrasonic testing. Section 4 summarises the findings followed by conclusions presented in Section 5.

2. Wavenumber mapping

The wavefield is first pre-processed so that only one mode at one frequency is left prior to wavenumber mapping. The instantaneous and local wavenumber techniques are then demonstrated and compared. The analysis by the local wavenumber technique is done using two types of windows, namely point- and line-wise moving windows. The wavefield used has been obtained from numerical modelling of guided wave propagation in a damaged aluminium plate.

2.1. Numerical modelling

A damage such as a delamination, impact or corrosion damage leads to a change in the wavenumber of a mode due to a thickness change. To demonstrate wavenumber mapping techniques the guided wave propagation was modelled in a 2 mm aluminium plate using the SHM module of the CIVA software, relying on a spectral finite element method for efficient simulations of the guided wave propagation [23,24]. The software relies on finite elements of order up to five to limit computational time. More details on the numerical modelling, such as time stepping and mesh size can be found in Ref. [25]. An overview of the numerical configuration is shown in Fig. 1. A "delamination" of

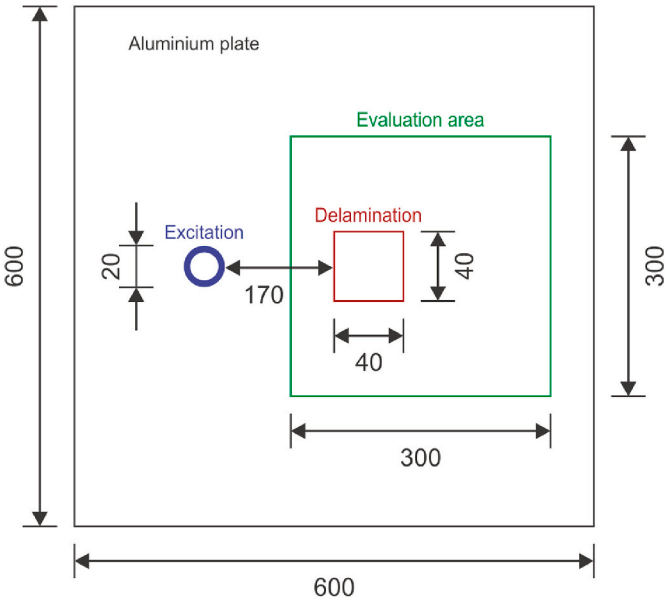

Fig. 1. Overview of the numerical model (not to scale).

dimension 20 × 20 mm^2 at the depth of 1 mm was modelled as a disconnection of the finite element nodes. This defect represents for example a lack of fusion in a stack of the aluminium sandwich, which could be observed in gluing operations. The material properties shown in Table 1 were used for modelling. The plate was excited by a three-cycle Hann-windowed burst at the centre frequency of 150 kHz applied as an axisymmetric ring-shaped excitation with the outer and inner diameter being 20 and 19 mm respectively, thus resulting in an effective width of 1 mm (see the blue ring in Fig. 1 marking the excitation area). This frequency is far below the cut-off frequencies of the higher-order modes, so that only S0 and A0 modes can propagate in the plate. A screenshot at 117.36 μs of the guided waves propagating in the plate and interacting with the damage is shown in Fig. 2a. At this time instant the S0 mode as a faster mode has already travelled to the right edge of the plate, reflected from it and travelled back to the damaged area again. The A0 mode as the slower mode almost passed the damaged area and its interaction with the damage is visible in the figure. Only the out-of-plane component is shown in Fig. 2a which is why the amplitude of the A0 mode is much larger than of the S0 mode.

2.2. Pre-processing of data

In order to estimate the defect depth through the wavenumber analysis, it is necessary to define a bijection between wavenumber and defect depth. For this purpose the Effective Thickness (ET) is defined, which is equal to the through-thickness distance between the inspected surface and the closest defect. Note that for pristine regions, the ET is locally equal to the thickness of the plate, while for delaminated or corroded areas, it highlights the depth of the delamination or the residual thickness of the plate, respectively. Due to a finite bandwidth of the excitation signal and the dispersive nature of guided waves, wavenumbers vary continuously with the frequency in the wavefield, hence this complicates quantitative depth analysis. Thus, it is advantageous not only to work with one mode but also with one frequency at which the mode is sensitive to the thickness changes. For this it is beneficial to analyse the dispersion curves for the given structure in advance. One example of the dispersion relation for the S0 and A0 modes at the excitation frequency of 150 kHz in the aluminium plate as a function of the ET is shown in Fig. 3. The relation was calculated in the Scaled Boundary Finite Element Method (SBFEM) [26] up to 8 mm thickness. It is apparent that the A0 mode is very sensitive to the thickness variation between 0.1 and 4 mm at this frequency. A smaller thickness leads to a higher wavenumber, and *vice versa*. From the thickness of 4 mm the difference between two respective wavenumbers in relation to the ET becomes smaller, so that it may be harder to estimate the actual thickness in this range. The wavenumber of the S0 mode stays almost constant with the thickness change, so that the S0 mode cannot be used for the estimation of ET.

To obtain one mode at a single frequency, additional signal processing [11] is necessary prior to wavenumber mapping which is summarised in the following and in Fig. 4. The 3DFFT is applied to the wavefield data, which allows to separate wavenumbers of propagating modes for each frequency by filtering in the wavenumber-frequency space. Having this data, the frequency of interest can be selected for further analysis, for instance the excitation frequency of 150 kHz in this case. Then, only the mode which is the most sensitive to the thickness variation is left by filtering other modes in wavenumber domain. The

Table 1
Material properties of aluminium, where E is Young's modulus, ν Poisson's ratio and ρ density.

Property	Value	Unit
E	70	GPa
ν	0.33	–
ρ	2770	kg m^{-3}

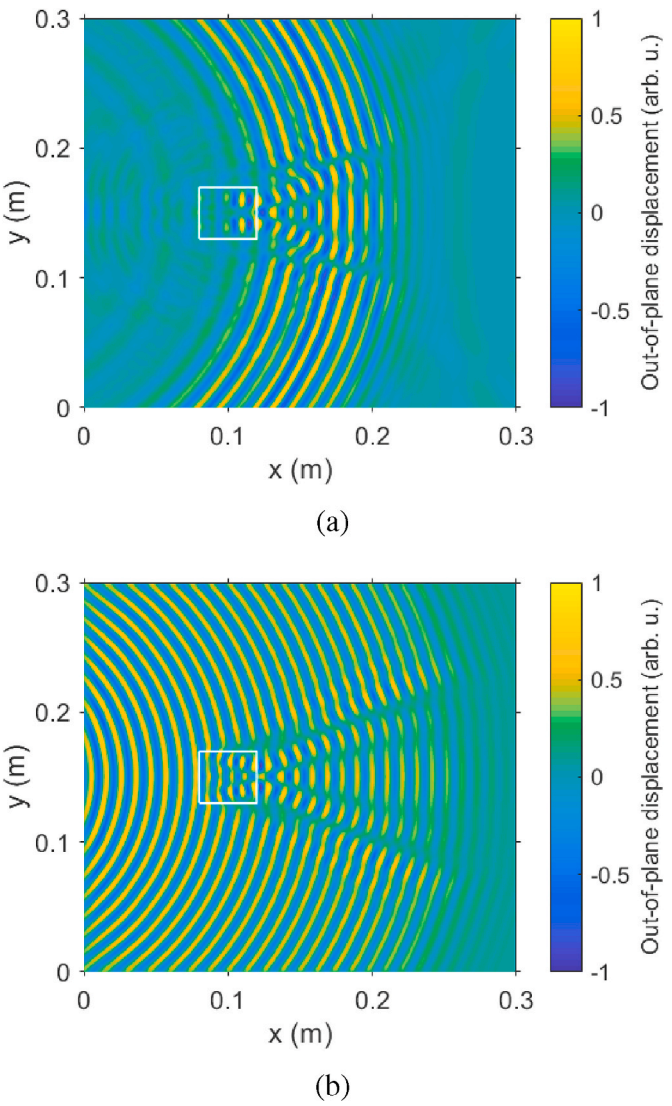

Fig. 2. (a) A screenshot of surface view at 117.36 μs of guided waves propagating and interacting with damage in a 2 mm aluminium plate modelled using the spectral element method and (b) a single frequency wavefield obtained using a pre-processing workflow shown in Fig. 4. The delamination is denoted by the white rectangle.

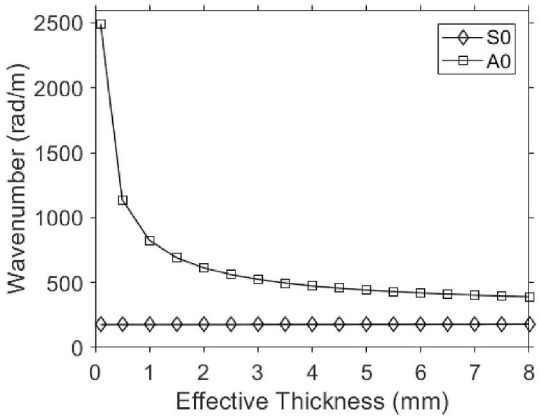

Fig. 3. Dispersion relation for the S0 and A0 modes at 150 kHz in the aluminium plate as a function of the Effective Thickness.

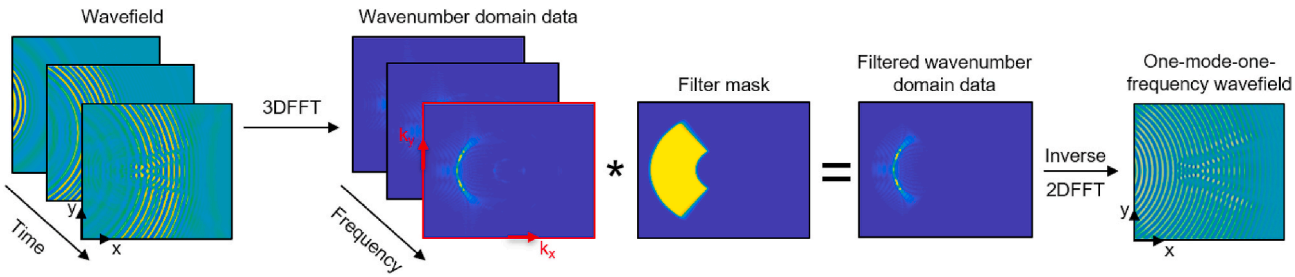

Fig. 4. Diagram showing the workflow for the pre-processing of wavefield data prior to wavenumber mapping.

filter is applied as a radial filter mask as it is shown in Fig. 4, where the yellow area is equal to 1 and dark blue area to 0. The edges are smoothed using a median filter to decrease artefacts. In the last step, the resulting frequency slice is transformed using the inverse 2DFFT to retrieve a single frequency wavefield, which is shown in Fig. 2b. The wavefield covers the entire region as if the plate was excited continuously. The length of the time signal prior to filtering is chosen so that there are no reflections from the plate edges which would disturb the wavefield and subsequently the wavenumber map, when calculated using the IW approach if no further filtering is applied. Note that the frequency selection could be done for every frequency contained within the excited bandwidth and in this work was limited to the centre excitation frequency to maximise signal-to-noise ratio (SNR).

All wavenumber mapping techniques described below were applied on the retrieved one-mode-one-frequency wavefield shown in Fig. 2b.

2.3. Instantaneous wavenumber

Mesnil et al. [19] differentiate between the Instantaneous Wavenumber (IW) and the Frequency Domain Instantaneous Wavenumber (FDIW). While the IW estimates the wavenumber from a wavefield at a single time instant, the FDIW measures it from a single frequency wavefield. The main difference lies in the reduction of data using a similar pre-processing procedure as shown in Fig. 4. The core mathematical operations to calculate the wavenumbers out of displacement (or particle velocity) are the same for both the IW and the FDIW techniques [27]. The short description of relevant steps is presented below, for more details the reader is referred to Ref. [27]. For the sake of brevity, the name Instantaneous Wavenumber (IW) will be used all along the paper and later compared to the Local Wavenumber (LW) mapping, which is a different approach for the wavenumber estimation.

To calculate the IW the analytical signal $g(x, y)$ of the wavefield $w(x, y)$ has to be calculated first. This is done by applying the Hilbert transform H to the wavefield data.

$$g(x,y) = w(x,y) + iH(w(x,y)) = A(x,y)e^{i\theta(x,y)} \tag{1}$$

The output of the transform are the amplitude $A(x, y)$ and the phase $\theta(x, y)$ of the wavefield. The next step is to take the first order derivatives of $\theta(x, y)$ along both spatial dimensions separately:

$$\begin{aligned} k_x(x,y) &= \frac{\partial\theta(x,y)}{\partial x} \\ k_y(x,y) &= \frac{\partial\theta(x,y)}{\partial y} \end{aligned} \tag{2}$$

The IW is calculated by the magnitude of $k_x(x, y)$ and $k_y(x, y)$:

$$IW(x,y) = \sqrt{k_x(x,y)^2 + k_y(x,y)^2} \tag{3}$$

Note that the time component is neglected here since the analysis is performed using the pre-processed data leaving one-mode-one-frequency wavefield. In the last step, the wavenumber map is filtered using a median filter to reduce the influence of the measurement noise and artefacts (high nonphysical wavenumbers at the phase discontinuities) prior to the calculation of the ET map. The size of the median filter used is 13 × 13 for both numerical and experimental cases.

2.4. Local wavenumber

The procedure for the LW mapping described here is similar to the mapping procedure, which was first described by Rogge et al. [17] and later used by Mesnil et al. [19] and Juarez et al. [20]. The basic idea of the approach is to multiply the wavefield data with a windowed function to be able to estimate the dominant wavenumber in a smaller region of the wavefield. In this paper, two types of windows are implemented, namely point- and line-wise moving windows. The sketch of the windows and their moving principles are shown in Fig. 5. The estimated wavenumber is assigned to the middle of the current region and the window is moved to the next region, *etc.* (this procedure is analogous to a short time FFT). The evaluation region and the assignment point for the point-wise moving window (pw) are shown in light and dark red colour in Fig. 5 (left), respectively. For the line-wise moving window (lw) shown in Fig. 5 (right), the evaluation region is at the overlap of both red and blue colours, whereas the resulting wavenumbers are assigned to the pixels shown with the dark red and blue colours for both spatial directions, respectively. Within the window, the spatially distributed displacements (particle velocities) are transformed using the 2DFFT for the point-wise window and 1DFFT for the line-wise window into the wavenumber domain so that the wavenumber with the highest amplitude can be estimated. The wavenumber with the highest amplitude is chosen in each window for the midpoint or midline, respectively. An important factor in the resolution of the techniques is the spatial window size. A trade of between spatial and wavenumber resolution has to be found: too large window results in the reduced spatial resolution, whereas too small window leads to poor wavenumber resolution [17, 20]. In this contribution the window size of twice the wavelength of the dominant mode was observed to provide adequate wavenumber resolution as in the work of Rogge and Leckey [17], and Juarez and Leckey [20]. In general, this is a good starting point, when damage is not known a priori and thus the mode wavelengths in the damage region cannot be predicted. Also, as it is done in the case of the IW, the LW map is filtered using the same median filter to reduce the influence of the measurement noise prior to the calculation of the ET maps.

2.5. Comparison of the techniques

Fig. 6 presents the wavenumber estimation results using the IW and LW with the point- and line-wise moving windows. The wavenumber maps clearly indicate the damage at its real position corresponding to its actual size very closely (highlighted with a white square). What happens is that the A0 mode propagating in the pristine region of the plate encounters the delaminated region where it splits into two independent modes, because the delaminated region is represented by two independent 1 mm plates. The dispersion relation shown in Fig. 3 is used to analyse the correctness of the estimated wavenumbers and later to convert them into the ET map. The A0 mode has the wavenumbers of 809 and 610 rad m^{-1} at the chosen frequency for the 1 and 2 mm plates,

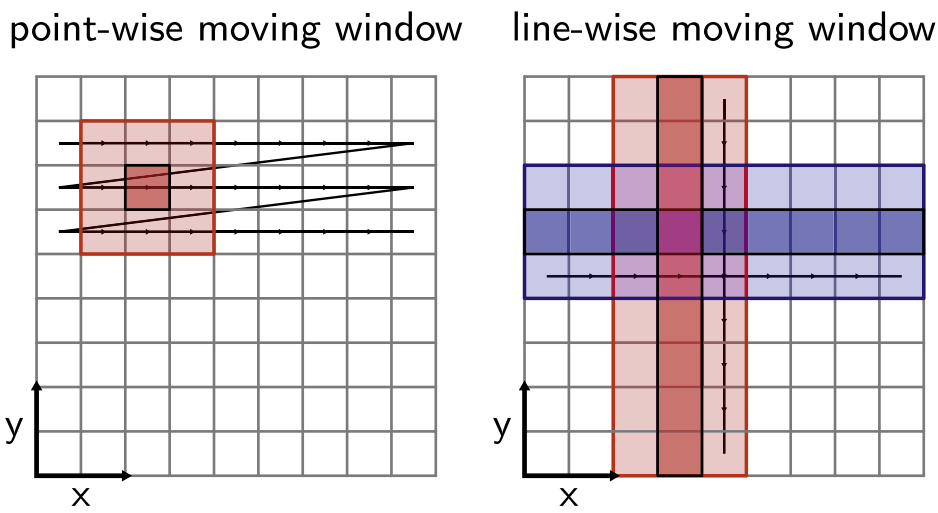

Fig. 5. Sketch representing two ways for the LW estimation, namely using the point- and line-wise moving windows. The evaluation region and the assignment point for the point-wise moving window (pw) are shown in light and dark red colour (left), respectively. For the line-wise moving window (lw) shown (right), the evaluation region is at the overlap of both red and blue colours, whereas the resulting wavenumbers are assigned to the pixels shown with the dark red and blue colours for both spatial directions, respectively. (For interpretation of the references to colour in this figure legend, the reader is referred to the Web version of this article.)

respectively. Thus, in the delaminated region the wavenumber of 809 rad m^{-1} is expected, whereas the pristine region should have the wavenumber of 610 rad m^{-1}. These wavenumbers are clearly identifiable in Fig. 6. Since the evaluation is performed at the plate's surface, only the upper 1 mm plate is visible on the wavenumber maps, and potential defects underneath are not observable with these techniques.

Using the dispersion relation of the A0 mode as a function of the ET shown in Fig. 3, the wavenumber map is converted into the ET map shown in Fig. 7. The defect depth with respect to the scanning surface of the plate is thus recovered. All three post-processing techniques closely indicate the actual size and depth of the delamination even though in the wave propagation direction the size is slightly over-estimated. The quantitative comparison of three wavenumber mapping approaches is presented in Fig. 8. Both LW approaches underestimate the damage depth resulting in 1.07 mm instead of 1 mm when compared to the IW and reference. This is due to the window size chosen for the LW mapping being twice the size of the wavelength expected in the pristine plate, which is bigger than that of the damaged area. Thus, wavenumbers at the damage area are smoothed more and the damage position across the thickness is estimated closer to the surface as it is. Moreover, none of the methods deliver uniform estimation of thicknesses, being it of the pristine plate or damaged area. In the edge regions of damage, the thickness estimation monotonously decreases from the thickness of the pristine plate to the thickness at which the damage is present resulting in overestimated in-plane size of damage. These results show the limitation in terms of the depth estimate of the techniques as it requires a large defect compared to the inspecting wavelength to be as small as possible for the transition regions (at the edge of the defect) to be captured precisely. Note the presence of the diagonal lines in the shadowed region behind the defect present for all three imaging techniques in Fig. 6, which are due to a phase discontinuity induced by the defect [27]. This artefact is very pronounced in the case of the IW and LW with a line-wise moving window, whereas the LW with a point-wise moving window is less susceptible to it. Finally, an almost vertical artefact is visible on the extreme right side of each map, which is due to the end of the modelling time before the A0 mode reaches the end of the inspected area as can be seen in Fig. 2b, hence the wavenumber values reach a discontinuity in this area.

The calculations were done in MATLAB for a 512 × 512 x 2048 wavefield data set on a 64-bit Windows 10 PC with 16 GB RAM. In terms of computational performance, the IW took 0.1 s to compute, whereas the LW with the point- and line-wise moving windows took 856 and 3 s, respectively. The high computational cost in the case of LW with the point-wise moving window is due to the zero padding inside the window (up to 512 points in both spatial directions).

3. Experimental results

In this section, the experimental set-up for conventional ultrasonic testing (UT) in immersion and wavefield measurements are described. The sample used is the aluminium-CFRP composite plate with the lay-up shown in Fig. 9 which was impacted at three locations from the CFRP-side. The impact damage in the plate is quantified using both UT and wavenumber mapping, followed by the comparison of the techniques.

3.1. Set-up

The sample for the experiments is a 480 × 480 × 6 mm^3 aluminium-CFRP composite plate, as can be seen in Fig. 9, build using resin transfer moulding process. The aluminium plate is 2 mm-thick and the CFRP plate of layup $[0/90]_3$ is 4 mm in thickness. A drop weight impact tester (IM10, IMATEK) was used to impact the plate from the CFRP-side at three different locations with the impact energies of 5, 10 and 30 J. The plate was impacted in its middle with the highest impact energy of 30 J which led to a plate deformation of a few millimetre at the aluminium side, but without perforation of the plate. Two smaller impacts were performed left and right from the centre of the 30 J impact laying on the diagonal 70 mm away.

3.1.1. Immersion testing

The scan was performed from the CFRP side using a focused 10 MHz PZT transducer (IAP10.20100E, Krautkrämer) with the focus at 100 mm, focal point of approx. 0.75 mm and diameter of 20 mm. The focusing was done at the specimen's surface. The sampling frequency was set to 100 MHz. The scan was centred on the middle of the sample and performed over an area of 240 × 240 mm^2 using a 1.2 mm step and 9 dB amplification.

3.1.2. Wavefield measurements

For the wavefield measurements, a 500 kHz broadband PZT transducer (Panametrics V101-RB Contact transducer, OLYMPUS) was glued 150 mm from the location of the main impact on the Al-side of the specimen. The excitation signal was a three-cycle burst at a centre excitation frequency of 100 kHz generated using a function generator (TG5011, AIM-TTI Instruments) and then amplified by a high-voltage amplifier (HVA-400-A, Ciprian) to 150 V before driving the transducer. The choice of excitation frequencies is motivated in subsection 3.3. The wavefield was recorded using a 3D scanning laser-Doppler vibrometer (PSV-500-3D-HV, Polytec). The experimental set-up for wavefield measurements is shown in Fig. 10. The scan areas were covered with a reflective spray to ensure the diffuse reflection. The

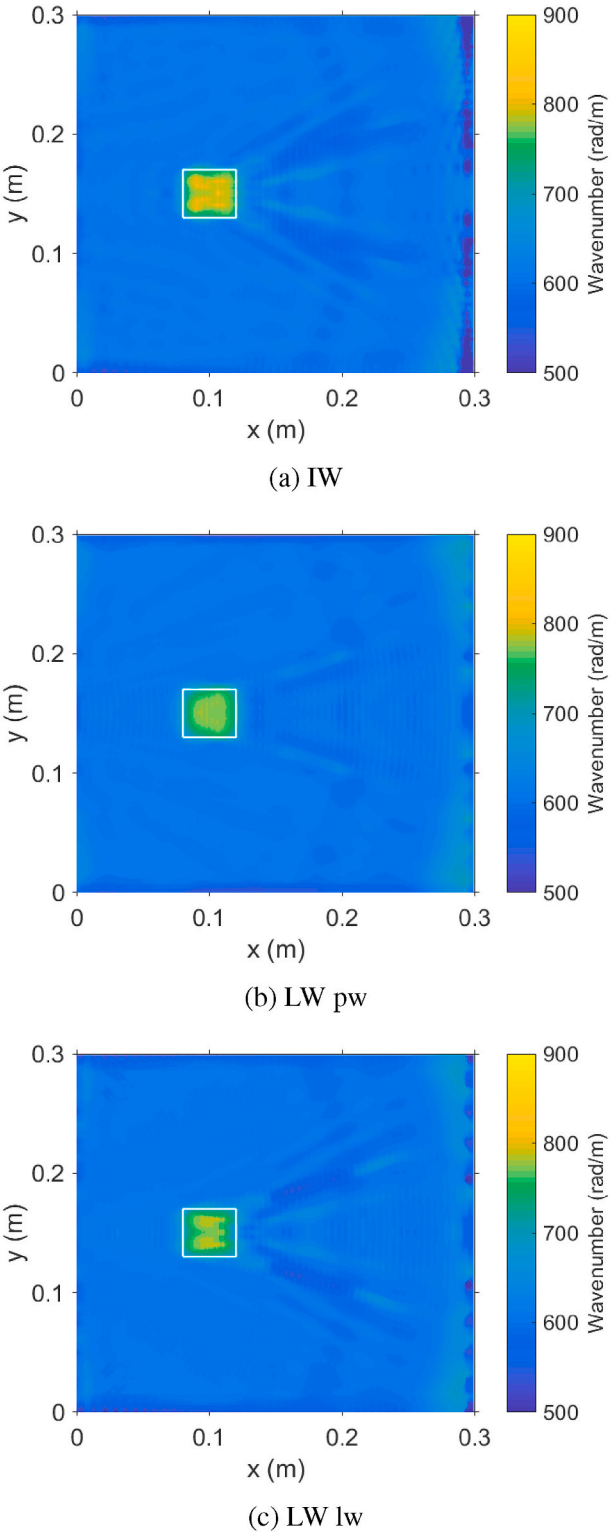

Fig. 6. Comparison of wavenumber estimation results using three wavenumber approaches. The delamination is denoted by the white rectangle.

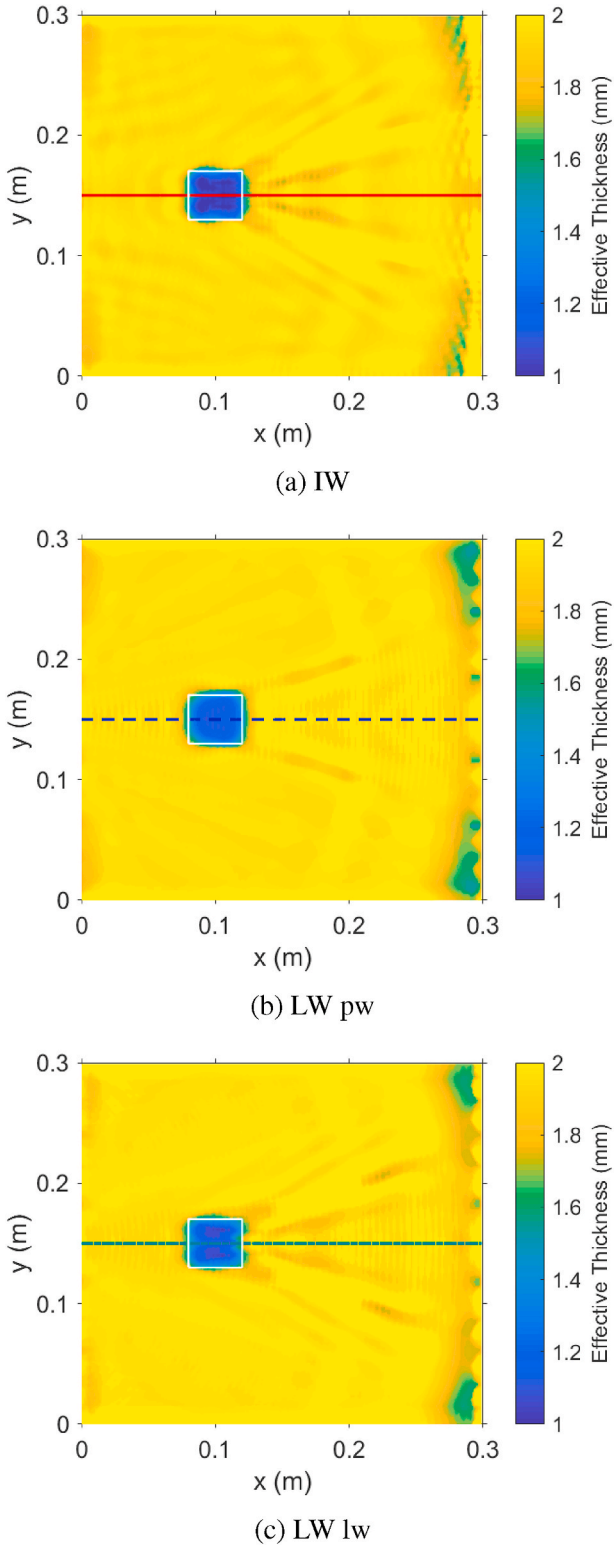

Fig. 7. Comparison of Effective Thickness estimation results based on three wavenumber approaches. The delamination is denoted by the white rectangle. Solid red, dashed blue and dashed-dotted green lines mark the position of cross-sectional cut which is presented in Fig. 8. (For interpretation of the references to colour in this figure legend, the reader is referred to the Web version of this article.)

sampling frequency of 3.125 MHz was used. The length of the recorded signals was 1.6 ms (5000 points). The scan area was approx. 220 × 220 mm^2 centred on the middle of the sample. The smallest possible scan grid resolution (in both spatial dimensions) for the measurements from the Al-side and CFRP-side were 0.8 and 0.81 mm, respectively. Since a 3D laser-Doppler vibrometer (3D LDV) is used, the scans on the Al-side and CFRP-side were aligned separately, thus they cannot be considered

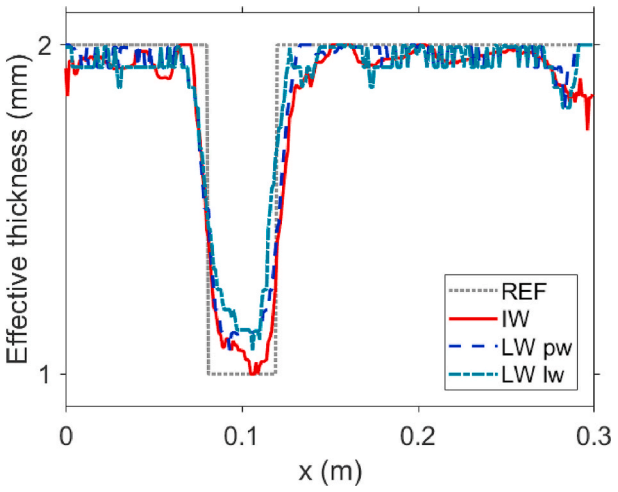

Fig. 8. Comparison of cross-sectional cuts of three wavenumber approaches from Fig. 7 to the reference.

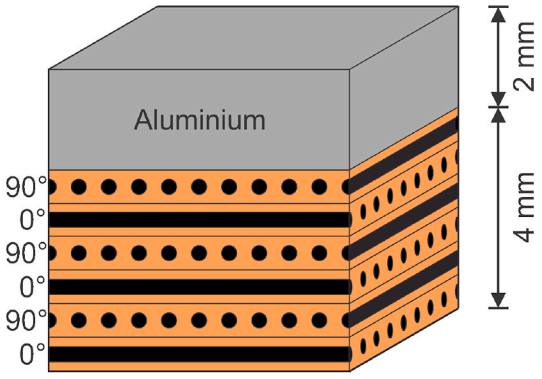

Fig. 9. A sketch of the aluminium-CFRP composite plate used in the experimental investigations.

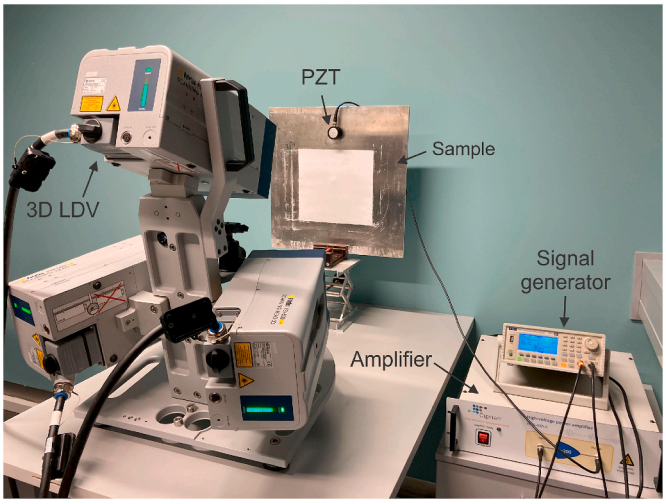

Fig. 10. Experimental set-up used for wavefield measurements.

identical. The smallest possible grid resolution is defined automatically by the system depending on the distance between the 3D LDV and the sample. Thus, one could achieve higher spatial resolution by bringing the sample closer to the 3D LDV, however, then it would not be possible to scan the area of the desired size. Only the out-of-plane velocity components were used for the wavenumber mapping.

3.2. Immersion testing analysis

The result from the immersion testing is shown in Fig. 11. This figure demonstrates the time of flight (ToF) in the aluminium-CFRP plate estimated with respect to the first wall echo (water/CFRP interface). Only two out of 3 impacts resulted in the visible damage in the CFRP layer as it can be seen in Fig. 11 (top) in the left-upper and right-bottom corners within the white dashed rectangle for 30 and 10 J, respectively. The biggest delamination is present at interface '6' and it seems that the damage due to the biggest impact of 30 J extends over the two other impacts of 5 and 10 J. The damage extent is 192 and 184.4 mm in the x- and y-directions, respectively. A typical pattern of delaminations between the CFRP plies can be observed in the case of the biggest impact of 30 J, see the left-upper corner of the enlarged view at the bottom in Fig. 11 [28]. The delaminations grow through the thickness of the plate and are visible at interfaces '1' through '2', as well as '5'. Only the delamination at interface '4' seems not to extend over delaminations from the previous interfaces and only tiny areas of it are visible. The total size of the impact damage of 30 J when considering the CFRP plies only is 54.4 and 32.8 mm in the x- and y-directions, respectively. The impact damage shape can be approximated as an ellipse according to

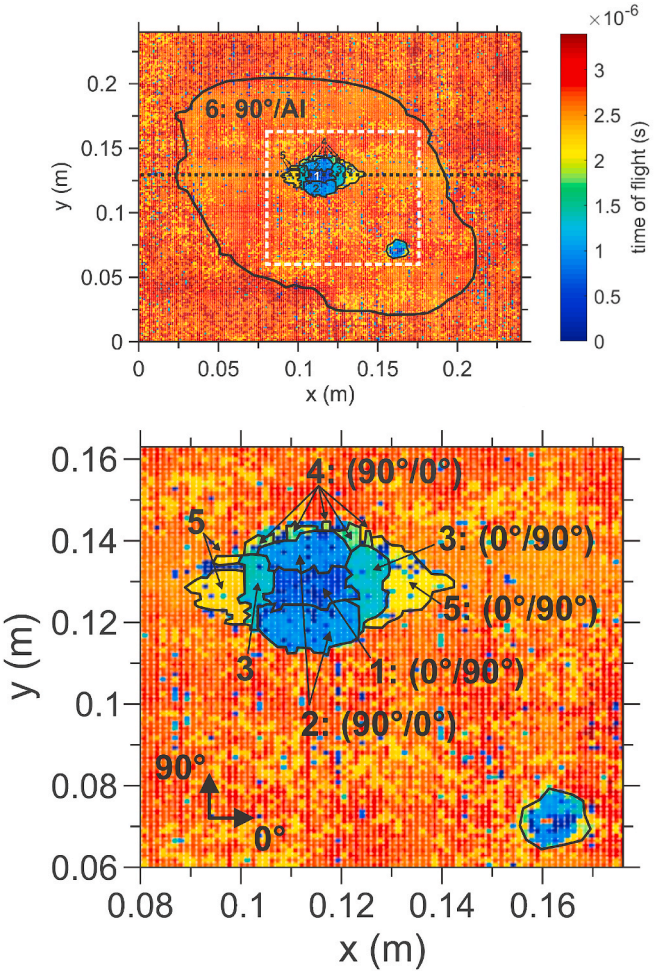

Fig. 11. A time-of-flight image (top) and its enlarged view (bottom) of the aluminium-CFRP plate obtained using immersion testing. The white dashed rectangle marks the area used for the enlarged view. Black dotted line marks the position of the cross-sectional cut which is presented in Fig. 17. Black solid lines mark contour of impact damage. Numbers show the interfaces at which delamination is present across the sample thickness as can be seen in Fig. 12.

Ref. [29] and thus the resulting area can be estimated and is equal to approx. 1400 mm^2. As for the damage cause by the 10 J impact, which can be seen in the right-bottom corner of the enlarged view at the bottom in Fig. 11, it is not possible to clearly identify the borders of interface delaminations due to its small size and the scan resolution used. The overall extent of this damage is 14.3 and 14.9 mm in the x- and y-directions, respectively, resulting in the area of approx. 167 mm^2.

3.3. Wavefield analysis

This subsection presents the wavefield analysis of the impact damage in the aluminium-CFRP composite plate. At first, the choice of excitation frequencies is motivated. Then, energy maps of the measured wavefields are presented and discussed. Next, wavenumber mapping approaches are compared to each other and to the reference measurement shown in subsection 3.2. Note that the same pre-processing of the data as described in subsection 2.2 and shown in Fig. 4 is applied prior to wavenumber mapping. Moreover, all wavenumber maps are filtered using the same median filter to reduce the influence of the measurement noise prior to the calculation of the ET maps.

3.3.1. Choice of excitation frequencies

To be able to select a centre excitation frequency wisely, dispersion curves for a given structure have to be calculated and analysed in advance. For this, elastic constants, density, plate layup and thickness have to be known. With the dispersion curves, one can find a trade-off between mode sensitivity to thickness changes and required spatial resolution. Typically, higher frequencies result in higher sensitivity to the thickness change, but they require smaller grid sizes to be able to resolve the smallest expected wavelength (highest wavenumber). According to Refs. [17,20,30] approximately ten spatial steps per wavelength are necessary to be able to resolve desired wavelength. Moreover, because of the asymmetry of the composite specimen used in this study two models have to be considered – one from the Al-side and one from the CFRP-side. Thus, two sets of dispersion curves are calculated to obtain the relationship between the ET and the wavenumber at the desired frequency. Using these relationships, a wavenumber map can be converted to an ET map, which will indicate the delamination depth present in the sample. In the pristine region the ET is equal to the total thickness of the aluminium-CFRP composite plate. In the delaminated region the value of the ET corresponds to the depth at which the delamination is present and is smaller than the total thickness of the hybrid composite plate. Since a delamination may only appear in-between plies, the ET values are discretised to match the number of interfaces. Fig. 12 shows the schematic of the wavenumber (wavelength) dependence on the thickness of the plate allowing for estimation of the delamination depth. Thus, seven ETs are considered – six for each interface plus one for the pristine plate. The interfaces are marked with respect to the CFRP-side. The calculations in the SBFEM were performed

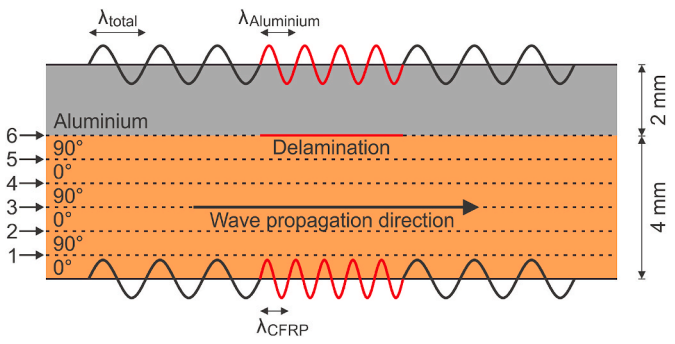

Fig. 12. Schematic showing dependence of damage depth (effective thickness) on the wavelength of guided waves. Interfaces are numbered from 1 to 6 with respect to the CFRP-side.

for seven composite plates made of a single CFRP ply, two CFRP plies, *etc.* up to the total thickness of the aluminium-CFRP composite plate. Material parameters listed in Tables 1 and 2 were used for the calculations.

Since the composite plate is not symmetric with respect to the middle plane the modes cannot be separated into antisymmetric and symmetric and only resemble S0 and A0 modes. Therefore, these modes are called the S0- and A0-like modes in the following. Fig. 13 presents the dispersion relation as a function of the ET for the A0-and S0-like modes considered with respect to the CFRP-side. Three frequencies are shown here, namely 100, 150 and 200 kHz. The calculated relations are non-monotonous meaning that the ET cannot be estimated uniquely for the case presented here. It is remarkable from Fig. 13 that the wavenumber increases when a 90° CFRP-layer is added to the composite plate (wavenumbers markered with arrows), while an addition of a 0° layer and aluminium plate leads to a wavenumber decrease. This behaviour appears for all presented as well as other frequencies and modes (not shown here) which allows to conclude that this non-monotonous relation comes from the plate's layup and its anisotropy. The difference in material properties and therefore in the behaviour of guided waves for 0° and 90° layers is so big in the case of CFRP that it leads to the non-monotonous relation between wavenumber and thickness shown in Fig. 13. Similar behaviour for CFRP was observed by Juarez and Leckey [20], which was not the case for the glass-fibre reinforced plastic composite studied by Mesnil et al. [19]. It can be observed from Fig. 13 that the A0-like mode is sensitive to thickness variation for all three frequencies. With the frequency increase, the wavenumbers considered with respect to the same thickness increase too. Moreover, the difference between the wavenumbers for one CFRP ply and aluminium-CFRP plate increases with the frequency, *e.g.* the wavenumber difference for 100, 150 and 200 kHz are 300, 374 and 423 rad m^{-1}, respectively. These differences were calculated based on the fitted values shown with the dashed lines in Fig. 13. To eliminate the ambiguity in the wavenumber-thickness relation, a quadratic interpolation of the wavenumbers was used. It would be very advantageous to use the frequency of 200 kHz, since it has the biggest variation of the wavenumbers with frequency, however, it would require a spatial resolution of approx. 0.6 mm, which is not possible with the current set-up. As for the frequencies of 100 and 150 kHz, the maximum expected wavenumbers are 700 and 970 rad m^{-1}, respectively. Thus, the spatial step of 0.81 mm from the measurement set-up results in 11 and 8 points per wavelength, respectively. Therefore, frequency of 100 kHz is chosen to fulfill the requirement of ten spatial steps per wavelength [17,20,30]. Moreover, for this complex experimental case, it is assumed that the ET-wavenumber relationship is monotonous, while for simpler composite with a bijective ET-wavenumber relationship, a discretised set of ET values corresponding to the plate layup could be used.

Regarding the dispersion relation considered with respect to the Al-side, the behaviour is the same as for the CFRP-side - an increase or decrease in wavenumbers can be observed when adding a 0° or 90° layer, respectively. The results are not shown here for brevity. However, the result from the conventional UT shown in Fig. 11 demonstrates that the biggest delamination is at the aluminium-CFRP interface (interface '6' in Figs. 11 and 12). It is expected that this delamination will hide all other smaller delaminations between the CFRP layers when measured

Table 2
Material properties of a single transverse isotropic ply, where $\mathbf{C_{ij}}$ are elastic constants and ρ is density (the direction 1 is along the fibres).

Property	Value	Unit
$\mathbf{C_{11}}$	98.914	GPa
$\mathbf{C_{12}}$	5.8036	GPa
$\mathbf{C_{22}}$	3.5143	GPa
$\mathbf{C_{23}}$	2.5767	GPa
$\mathbf{C_{55}}$	3.5887	GPa
ρ	1446	kg m^{-3}

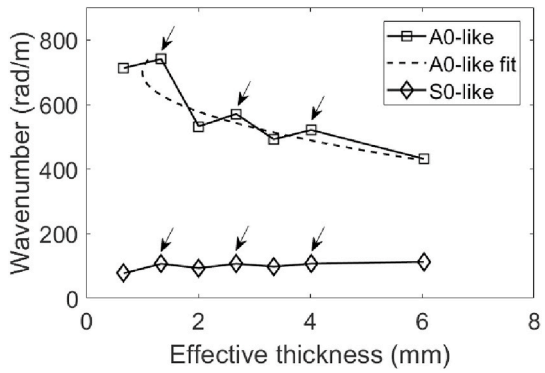

(a) 100 kHz

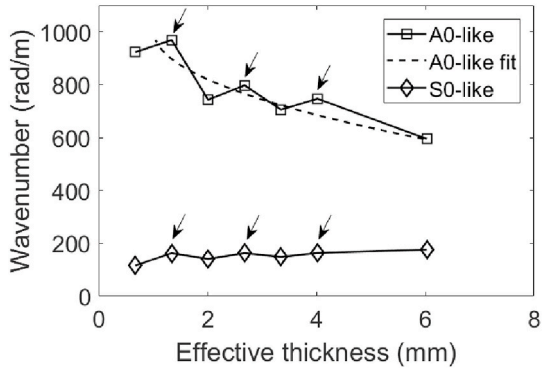

(b) 150 kHz

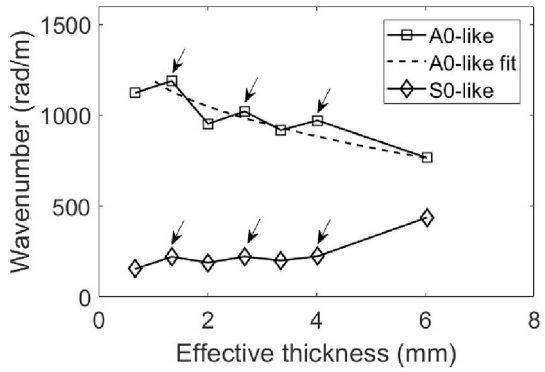

(c) 200 kHz

Fig. 13. Dispersion relations of the A0-and S0-like modes at different frequencies as a function of the Effective Thickness. The relations are calculated with respect to the CFRP-side. The arrows mark the wavenumbers resulting from the addition of a 90◦ CFRP-layer.

from the Al-side due to the shadowing effect. Thus, the model can be simplified by considering only two ET and two respective wavenumbers for one frequency. The biggest difference of 50 rad m^{-1} between two wavenumbers is found to be for 100 kHz. For the other two frequencies of 150 and 200 kHz, the differences in wavenumbers are smaller and equal to 15 and 39 rad m^{-1}, respectively. Therefore, 100 kHz is used in the experiments as the centre excitation frequency. The expected wavenumbers are 432 rad m^{-1} for the 6 mm pristine aluminium-CRRP composite plate and 482 rad m^{-1} for the 2 mm aluminium plate, both of which can be resolved with the spatial step of 0.8 mm defined by the measurement set-up.

3.3.2. Energy maps

Energy maps of the measured wavefields were calculated by taking the weighted root mean square (WRMS) value of the time signals at each spatial point as it is done in Ref. [31]:

$$\mathrm{WRMS}(x,y) = \sqrt{\frac{1}{N}\sum_{n=1}^{N} w(x,y,t_n)^2 \cdot n^q}, \tag{4}$$

where w is the wavefield and q is a positive weighting factor. This factor is automatically calculated by the approach of [31]. The weighting function n^q in the WRMS compensates the attenuation. The signal is cut to the part with a relevant amplitude because the weighting function is rapidly increasing for a longer signal. Alternatively, a geometric weighting could be applied [32] which require the exact transducer position. The resulting WRMS-maps for two measurements - on the Al-side and CFRP-side - are presented in Fig. 14 for the centre excitation frequency of 100 kHz. The biggest delamination at interface '6' becomes visible in both measurements (confer Figs. 14–11). Additionally, the damaged area at the site of the biggest impact becomes visible in the middle of the scanned area for the measurement performed on the CFRP-side, see red colour approx. in the middle of the scan having WRMS values around 0.35 mm s^{-1} in Fig. 14b. This high amplitude when compared to the rest of the damaged area (at interface '6') is due to the mode trapping between delamination boundaries. The smaller impact damage visible in the reference measurement (Fig. 11) is not observed in the WRMS maps (Fig. 14). It is very interesting to observe that the WRMS values increase at the delamination at interface '6' compared to the pristine plate, as it can be seen in Figs. 14b and a for the

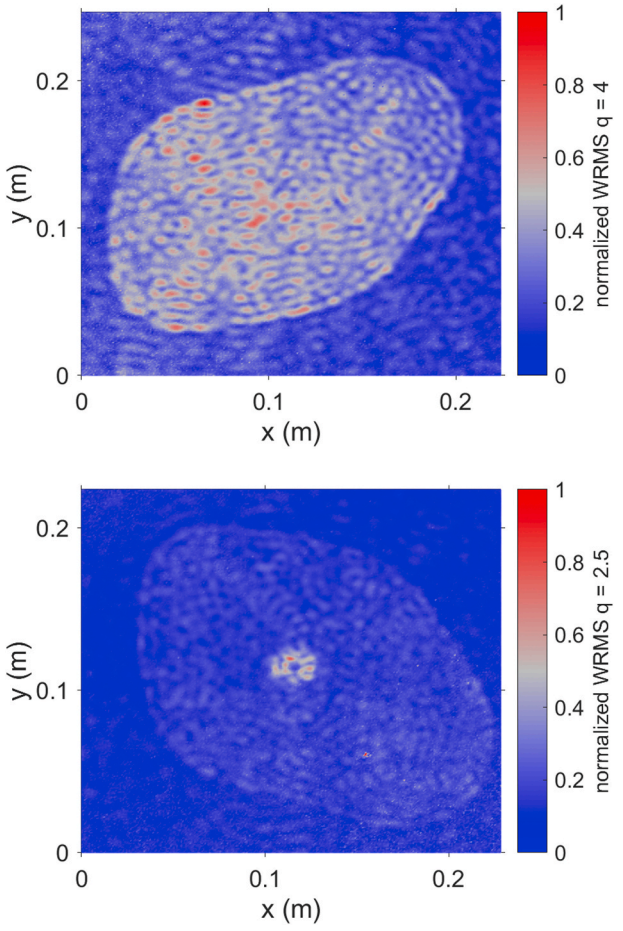

Fig. 14. WRMS-maps for the measurement on the (a) Al-side and (b) CFRP-side at the centre excitation frequency of 100 kHz.

measurement on the CFRP- and Al-sides, respectively. This is possibly due to the amplitude of A0 mode being higher in this frequency range in the pure aluminium plate and the CFRP stack when compared to the amplitude of A0-like mode propagating in the pristine aluminium-CFRP plate. The SNR were calculated for both measurements and are equal 22 dB (Al-side) and 18 dB (CFRP-side). The difference between the SNR is a factor of 1.8.

3.3.3. *Wavenumber mapping from the CFRP side*

Fig. 15a shows interaction of the S0- and A0-like modes with the impact damage measured at the CFRP side at 366.4 μs. The S0-like mode is faster, has bigger wavelength and lower amplitude than the A0-like mode. At this instant of time the S0-like mode is all over the scanned region, whereas the A0-like mode just arrives at the left edge of the delaminated region. Moreover, the propagation of the S0-like mode over the delamination leads to a mode conversion to the A0-like mode. The converted mode scatters in all directions and highlights the delamination contour. Note that the mode and frequency filtering described previously will incorporate the mode contribution from both the incident and converted (from S0-like mode) A0-like mode, as the wavenumber within the delamination should be equal for both phenomena.

The pre-processing of the data was done in the same way as for the aluminium plate (see Fig. 4) such that the one-mode-one-frequency wavefield can be obtained. The only difference is that wavenumbers

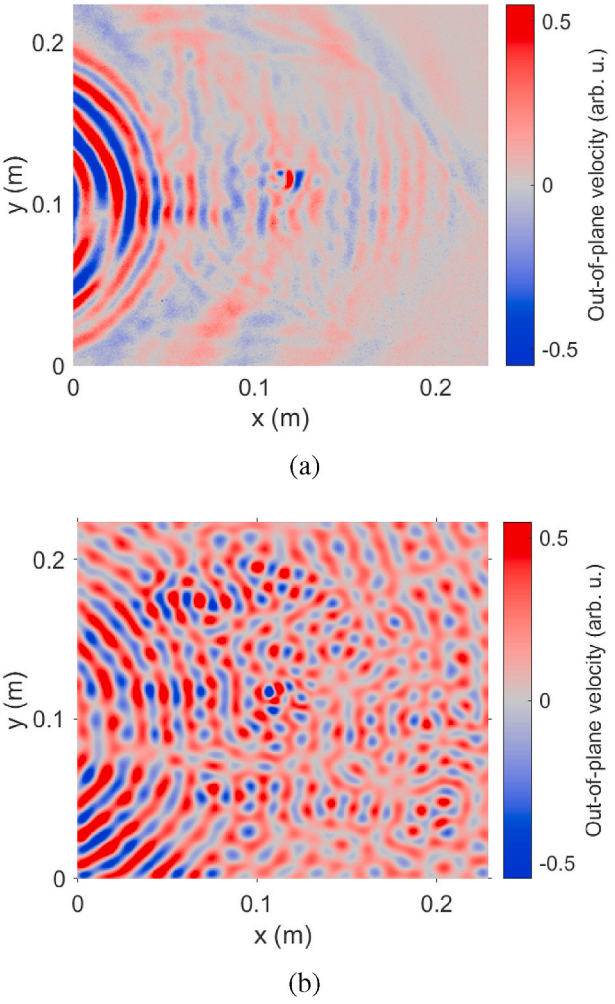

Fig. 15. Interaction of the excited modes with the impact damage measured from the CFRP side. (a) Original snapshot of the wavefield at 366.4 μs and (b) the 100 kHz frequency A0-like-only wavefield obtained using a pre-processing workflow shown in Fig. 4.

for the A0-like mode were taken for every direction (360°) to capture the scattering at the delamination which as well happens in every direction. Time signals were cut in the beginning and at the end (where only noise is present), but without reducing the time resolution, to be able to calculate the 3D FFT in MATLAB for a 512 × 512 x 4096 wavefield data set. The calculations were done on a 64-bit Windows 10 PC with 32 GB RAM. The resulting wavefield is shown in Fig. 15b to which the wavenumber mapping algorithms are then applied. The wavenumber maps are presented in Fig. 16. While the impact damage is not observable in the single frequency wavefield in Fig. 15b, every wavenumber map presented in Fig. 16 highlights the size and shape of the damage. The most uniform damage indication is delivered by LW approach with the point-wise window (Fig. 16b), because it is insensitive to the directional information of scattered waves. The estimated wavenumbers of the pristine region are between 380 and 419 rad m^{-1}. In the case of the delaminated region (at interface '6') the wavenumbers are spread between 470 and 559 rad m^{-1}. In the middle of the scanned area the highest wavenumber of 676 rad m^{-1} is observed. The fitted dispersion relation shown with the dashed-line in Fig. 13a is applied to the wavenumber maps to retrieve the ET maps presented in Fig. 18. The shape of the damage obtained using the guided wave-based wavenumber analysis deviates from the ones using the conventional UT and WRMS-mapping, to be seen in Figs. 18, 11 and 14b, respectively. The ET maps using the three different approaches estimate correctly the total thickness of the plate in most of the pristine region, as to be seen in yellow colour for the thickness of 6 mm in Fig. 18. For the whole delaminated region, blue, green and orange colours are present, corresponding to the thickness values around 2, 4 and 4.5 mm, respectively. The largest delaminated region is at the aluminium-CFRP interface (marked '6' in Fig. 11), thus the expected value for the ET should be 4 mm which correlates with the estimate obtained from the ET maps (see green colour in Fig. 18). Also, the ET maps indicate delamination damage in the middle which lie closer to the surface of the CFRP for the ET values between 1.1 and 2.94 mm, see blue and light blue colours in Fig. 18, respectively. However, no clear indication of multiple delaminations (due to the biggest impact) and their shape can be observed, as it can be done for the measurements using conventional UT. Moreover, there is no indication of other impact damage, which is expected in the right-bottom area (Fig. 18). Note orange colour visible in the damaged region, corresponding to the ET of approx. 4.5 mm, which is impossible in this case because the aluminum plate has no damage in it. This comes from the continuous wavenumber-ET relation considered in this work, the wavenumber between 490 and 430 rad m^{-1} get assigned to the thickness values between 4 and 6 mm (see Fig. 13a).

To analyse the wavenumber results more quantitatively, a cross section view has been added in Fig. 17 and shows the overlap of the three wavenumbers techniques with the pulse-echo time of flight measured by conventional UT. Note that the alignment has been made by hand as the immersion testing and wavefield measurement do not have the same coordinate system. Furthermore, the y-scale of wavenumber and time of flight are not directly comparable. Indeed, if the time of flight variation is linear with the depth of the defect, this is not the case of the wavenumber values (as shown in Fig. 13). Nevertheless, all three wavenumber techniques succeed to detect at the appropriate location the shallower defect, *i.e.* shortest time of flight (called defect peak in the following), with sensibly similar extreme values. If the x-extent of this damage peak seems better described by the IW, this result might not be generalisable. On the left hand side, *i.e.* between the wave excitation and the defect peak, the wavenumber estimate is very constant spatially and equal for three techniques. This is not the case on the right hand side of the defect, where the IW and LW lw results oscillate while the LW pw seems to overestimate the wavenumber but is relatively constant. The difference between right and left sides with respect to the damage peak can be either attributed to the scattered waves from the damage peak (*i.e.* a shadowing effect) or to the lower amplitude of the wave due to attenuation. Moreover, the fact that the wavenumbers

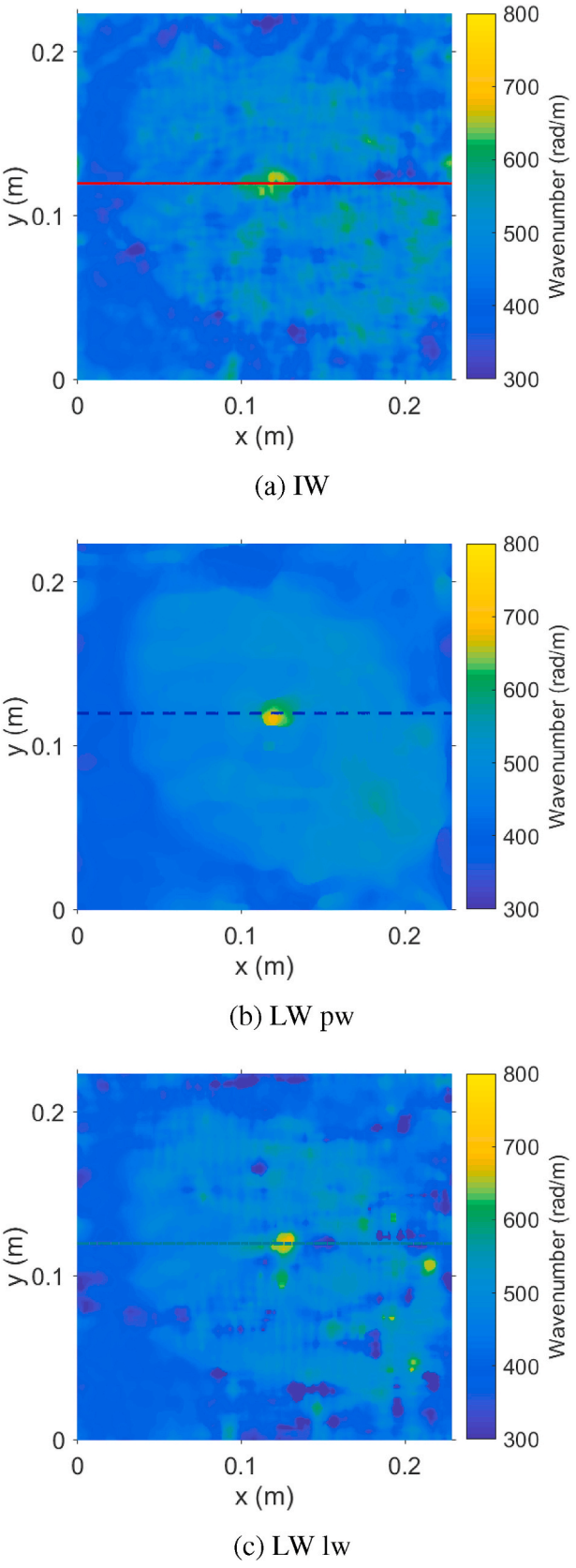

Fig. 16. Comparison of wavenumber estimation results for the aluminium-CFRP plate while scanning on the CFRP-side. Solid red, dashed blue and dashed-dotted green lines mark the position of cross-sectional cut which is presented in Fig. 17. (For interpretation of the references to colour in this figure legend, the reader is referred to the Web version of this article.)

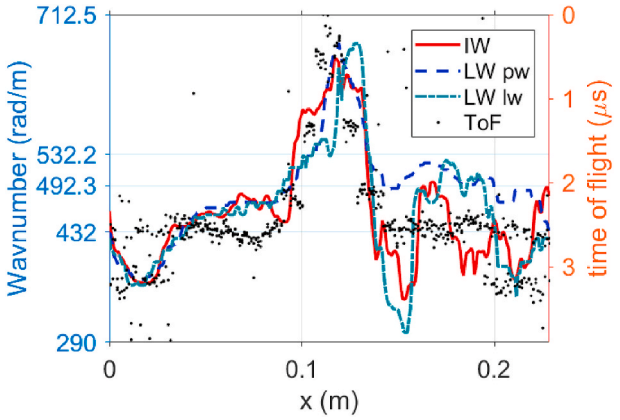

Fig. 17. Comparison of cross-sectional cuts of three wavenumber approaches from Fig. 16 and conventional UT from Fig. 11.

are equal but slightly over the expected 432 rad m^{-1} value on the left side of the defect peak might indicate the shortcoming of the model described in Fig. 12 with respect to effective ply thickness and material properties.

In terms of computational performance, the IW took 0.1 s to compute, whereas the LW with the point- and line-wise moving windows took 676 and 2.1 s, respectively. The high computational cost in the case of LW with the point-wise moving window is due to the zero padding inside the window (up to 512 points in both spatial directions).

3.3.4. *Wavenumber mapping from the aluminium side*

Fig. 19 shows the ET maps calculated for the measurement performed on the Al-side, while the wavenumber maps are not presented here for the sake of brevity. It is not possible to clearly identify the shape of the damage from the ET maps as in the case of the analysis performed from the CFRP side (confer Figs. 19 and 18). The ET maps for the measurement performed on the Al-side are distorted showing that aluminium is delaminated from the CFRP in different regions of the area scanned, see blue colour in Fig. 19. The poor result with respect to the aluminium side probably comes from the measurement noise and the close relation (the difference of 50 rad m^{-1}) between wavenumbers for the pristine composite and aluminium plate. Note that in the case of the LW with the point-wise moving window shown in Fig. 19b a similar damage pattern appears as for the ET maps estimated from the CFRP-side in Fig. 18, however, which is much harder to recognise without knowing the shape in advance.

Finally, the LW with the point-wise moving window took 756.3 s to compute, while the IW and LW with the line-wise moving window required 0.1 and 2.3 s, respectively.

4. Summary

In this contribution, the instantaneous and local wavenumber imaging techniques were compared, the latter being implemented using two types of windows. The techniques were demonstrated on a numerical example of a damaged aluminium plate first, before their application to an experimental case. For the numerical case, all three approaches showed similar performance in terms of quantification of damage size and depths. The in-plane size of damage was slightly overestimated in the direction of the incidence wave for all approaches.

For the experimental case, an aluminium-CFRP composite plate with impact damage was measured and analysed. This structure corresponds to composite pressure vessels with a load-sharing metal liner used for storing gases in aerospace and automotive industries. Due to assymmetry of the plate, two cases were considered - for the measurements performed from the CFRP- and Al-sides. The WRMS-maps for both measurements revealed the biggest delamination present between

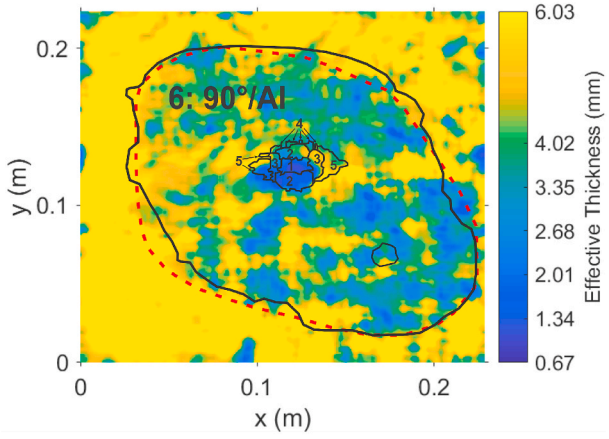

(a) IW

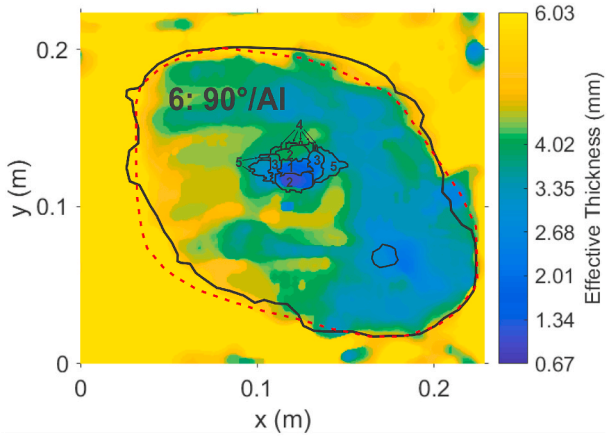

(b) LW pw

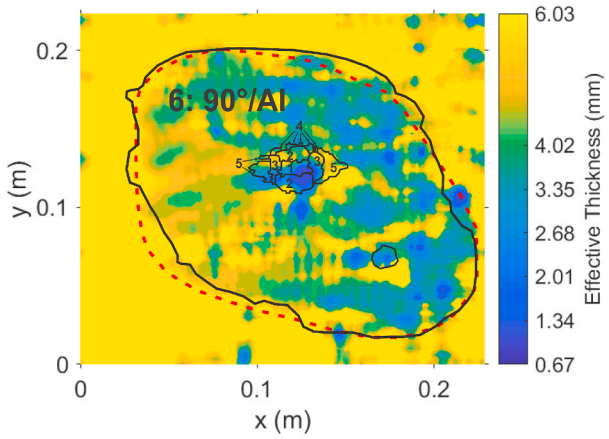

(c) LW lw

Fig. 18. Comparison of Effective Thickness estimation results for the aluminium-CFRP plate while scanning on the CFRP-side based on three wavenumber mapping techniques. Black and red dashed lines show the damage contours extracted from the UT (Fig. 11) and WRMS-maps (Fig. 14b), respectively. (For interpretation of the references to colour in this figure legend, the reader is referred to the Web version of this article.)

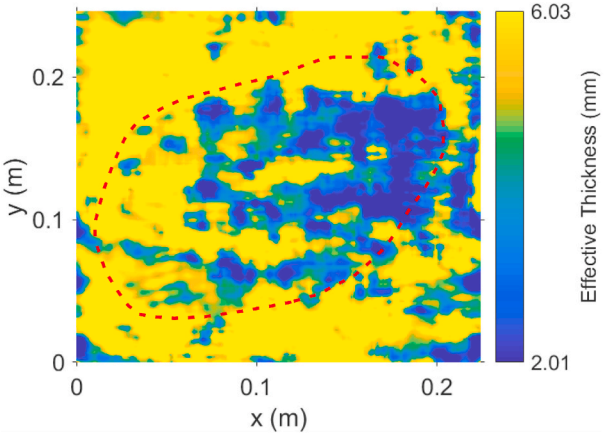

(a) IW

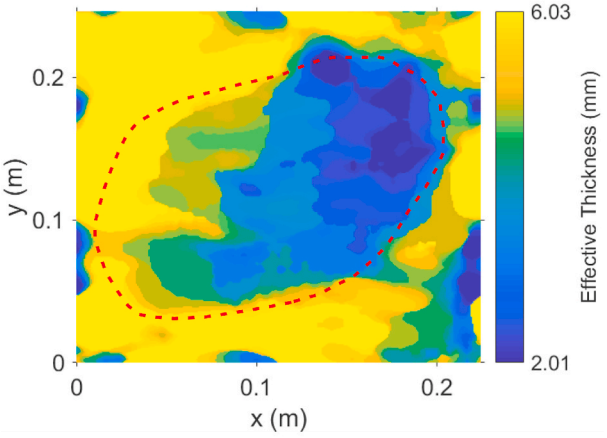

(b) LW pw

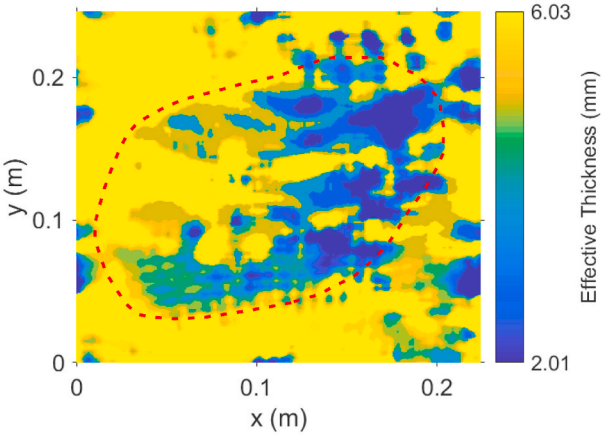

(c) LW lw

Fig. 19. Comparison of Effective Thickness estimation results for the aluminium-CFRP plate while scanning on the Al-side based on three wavenumber mapping techniques. The red dashed line shows the damage contour extracted from the WRMS-map (Fig. 14a). (For interpretation of the references to colour in this figure legend, the reader is referred to the Web version of this article.)

aluminium and CFRP parts. As for the wavenumber mapping for the measurement from the CFRP-side, it has also revealed the biggest delamination between aluminium and CFRP parts, as well as delivered an indication of impact damage in the CFRP part. In general, the damage

quantification results from the wavenumber mapping techniques are in a good agreement with the results from conventional ultrasonic testing. All techniques delivered similar estimations of the in-plane size and depth of the biggest delamination present between aluminium plate and CFRP part. The main limitation of the approach presented here is that it was not possible to quantify every delamination between CFRP plies caused by the impact as it is the case for conventional UT. Only some parts of the impact damage are visible in the wavenumber and thickness maps. Another limitation is that the relation between wavenumber and effective thickness is non-monotonous, which is due to the complexity of the layup of the composite plate used in the experiments and its anisotropy. In this work, a quadratic interpolation of the wavenumbers was used to eliminate this ambiguity, however, another approach, *e.g.* as presented by Juarez and Leckey [20] may be more beneficial to use for this purpose. In their approach, wavenumber estimation results for multiple frequencies are correlated in an effort to retrieve true depth information.

Even though the WRMS-map delivered a clear indication of the biggest delamination, it was not possible to clearly identify the damage shape and size using wavenumber mapping in the case of the measurement from the Al-side. This is due to the close relation between wavenumbers for the pristine composite plate and aluminium plate delaminated from it. The closest estimate in terms of shape and in-plane size of the damage was delivered by the local wavenumber approach with the point-wise window.

5. Conclusions

Wavenumber mapping has been shown to provide estimates of size, depth and location of impact damage in the aluminium-CFRP composite plate. The methodology can be seen as an NDE part of a hybrid SHM/NDE approach being reported in Ref. [33]. The idea is that an SHM system gives information of possible damage locations, which are then closely inspected using guided wave-based wavenumber mapping to quantify damage size and depth. In this paper, a transducer was glued to the specimen's surface for the excitation and a scanning laser-Doppler vibrometer was used for wavefield acquisition. However, a fully non-contact inspection is possible by utilising a laser [16] or an air-coupled transducer for the excitation. Even though, a relatively large impact damage has been investigated, the wavenumber analysis can be scaled to damage which size is in the order of a wavelength or larger [16]. Note that the smaller wavelengths would typically require higher frequencies which lead to considerably higher measurement time due to increased spatial sampling. Moreover, more modes exist at higher frequencies which may not be well-separated in the wavenumber domain thus complicating the wavenumber analysis.

Overall the wavenumber mapping techniques presented in this work show an excellent defect sensitivity and a reasonable defect quantification performance, therefore constituting a remote and contact-free measurement alternative to conventional ultrasonic testing. The lower frequency guided wave inspection also brings advantages compared to higher frequency bulk waves, especially for material exhibiting a frequency-dependent behaviour (attenuation, scattering …).

Supplementary material

The MATLAB scripts for obtaining the wavenumber and effective thickness maps with an example of the damaged aluminium plate are freely available online as a part of Open-Source Strategy of Bundesanstalt für Materialforschung und -prüfung [34]. The project can be downloaded at https://github.com/BAMresearch/WavenumberAnalysis.

CRediT authorship contribution statement

Yevgeniya Lugovtsova: Conceptualization, Methodology, Data acquisition, Investigation, Visualization, Data curation, Writing – original draft. **Jannis Bulling:** Software, Visualization, Data curation, Writing – review & editing. **Olivier Mesnil:** Conceptualization, Methodology, Software, Writing – review & editing. **Jens Prager:** Supervision, Writing – review & editing. **Dirk Gohlke:** Data acquisition. **Christian Boller:** Supervision, Writing – review & editing.

Declaration of competing interest

The authors declare that they have no known competing financial interests or personal relationships that could have appeared to influence the work reported in this paper.

Acknowledgements

The authors would like to thank Dustin Nielow from the Mechanics of Polymers division at BAM for the sample manufacturing. The authors are also immensely grateful to Dr Olaf Kahle from Fraunhofer IAP for providing his expertise and the impact testing facilities that greatly assisted the research. The authors gratefully acknowledge the DFG funding (project number 428590437).

References

[1] Koniuszewska AG, Kaczmar JW. Application of polymer based composite materials in transportation. Prog Rubber Plast Recycl Technol 2016;32(1):1–24. https://doi.org/10.1177/147776061603200101.
[2] Bunsell AR. Composite pressure vessels supply an answer to transport problems. Reinforc Plast 2006;50(2):38–41. https://doi.org/10.1016/S0034-3617(06)70914-6.
[3] Rajak DK, Pagar DD, Kumar R, Pruncu CI. Recent progress of reinforcement materials: a comprehensive overview of composite materials. Journal of Materials Research and Technology 2019;8(6):6354–74. https://doi.org/10.1016/j.jmrt.2019.09.068.
[4] Guo N, Cawley P. The interaction of lamb waves with delaminations in composite laminates. J Acoust Soc Am 1993;94(4):2240–6. https://doi.org/10.1121/1.407495.
[5] Glushkov E, Glushkova N, Golub MV, Moll J, Fritzen C-P. Wave energy trapping and localization in a plate with a delamination. Smart Mater Struct 2012;21(12):125001. https://doi.org/10.1088/0964-1726/21/12/125001.
[6] Żak A, Radzieński M, Krawczuk M, Ostachowicz W. Damage detection strategies based on propagation of guided elastic waves. Smart Mater Struct 2012;21(3):035024. https://doi.org/10.1088/0964-1726/21/3/035024.
[7] Yu L, Leckey CA. Lamb wave–based quantitative crack detection using a focusing array algorithm. J Intell Mater Syst Struct 2013;24(9):1138–52. https://doi.org/10.1177/1045389X12469452.
[8] Ren B, Lissenden CJ. Ultrasonic guided wave inspection of adhesive bonds between composite laminates. Int J Adhesion Adhes 2013;45:59–68. https://doi.org/10.1016/j.ijadhadh.2013.04.001.
[9] He S, Ng C-T. Guided wave-based identification of multiple cracks in beams using a bayesian approach. Mech Syst Signal Process 2017;84:324–45. https://doi.org/10.1016/j.ymssp.2016.07.013.
[10] Shen Y, Cen M. Delamination detection in composite plates using linear and nonlinear ultrasonic guided waves. ASME international mechanical engineering congress and exposition, vol. 9; 2019. https://doi.org/10.1115/IMECE2019-10928.
[11] Ruzzene M. Frequency–wavenumber domain filtering for improved damage visualization. Smart Mater Struct 2007;16(6):2116–29. https://doi.org/10.1088/0964-1726/16/6/014.
[12] Sohn H, Dutta D, Yang J, Park H, DeSimio M, Olson S, Swenson E. Delamination detection in composites through guided wave field image processing. Compos Sci Technol 2011;71(9):1250–6. https://doi.org/10.1016/j.compscitech.2011.04.011.
[13] Sohn H, Dutta D, Yang JY, DeSimio M, Olson S, Swenson E. Automated detection of delamination and disbond from wavefield images obtained using a scanning laser vibrometer. Smart Mater Struct 2011;20(4):045017. https://doi.org/10.1088/0964-1726/20/4/045017.
[14] Michaels TE, Michaels JE, Ruzzene M. Frequency–wavenumber domain analysis of guided wavefields. Ultrasonics 2011;51(4):452–66. https://doi.org/10.1016/j.ultras.2010.11.011.
[15] Yu L, Leckey CAC, Tian Z. Study on crack scattering in aluminum plates with lamb wave frequency–wavenumber analysis. Smart Mater Struct 2013;22(6):065019. https://doi.org/10.1088/0964-1726/22/6/065019.
[16] Flynn EB, Chong SY, Jarmer GJ, Lee J-R. Structural imaging through local wavenumber estimation of guided waves. NDT E Int 2013;59:1–10. https://doi.org/10.1016/j.ndteint.2013.04.003.
[17] Rogge MD, Leckey CA. Characterization of impact damage in composite laminates using guided wavefield imaging and local wavenumber domain analysis. Ultrasonics 2013;53(7):1217–26. https://doi.org/10.1016/j.ultras.2012.12.015.

[18] Tian Z, Yu L, Leckey C. Delamination detection and quantification on laminated composite structures with lamb waves and wavenumber analysis. J Intell Mater Syst Struct 2015;26(13):1723–38. https://doi.org/10.1177/1045389X14557506.
[19] Mesnil O, Leckey CA, Ruzzene M. Instantaneous and local wavenumber estimations for damage quantification in composites. Struct Health Monit 2015;14(3):193–204. https://doi.org/10.1177/1475921714560073.
[20] Juarez PD, Leckey CA. Multi-frequency local wavenumber analysis and ply correlation of delamination damage. Ultrasonics 2015;62:56–65. https://doi.org/10.1016/j.ultras.2015.05.001.
[21] Jeon JY, Gang S, Park G, Flynn E, Kang T, Han SW. Damage detection on composite structures with standing wave excitation and wavenumber analysis. Adv Compos Mater 2017;26(sup1):53–65. https://doi.org/10.1080/09243046.2017.1313577.
[22] Lugovtsova Y, Mesnil O, Bulling J, Prager J, Boller C. Damage quantification in aluminium-cfrp composite structures using guided wave wavenumber mapping. In: AeroNDT 2019 conference proceedings; 2020, 050018. 11th International Symposium on NDT in Aerospace, Nov 2019, Paris-Saclay, France.
[23] Mesnil O, Imperiale A, Demaldent E, Chapuis B. Validation of spectral finite element simulation tools dedicated to guided wave based structure health monitoring. AIP Conference Proceedings 2019;2102(1):050018. https://doi.org/10.1063/1.5099784.
[24] A. Imperiale, N. Leymarie, E. Demaldent, Numerical modeling of wave propagation in anisotropic viscoelastic laminated materials in transient regime: application to modeling ultrasonic testing of composite structures, Int J Numer Methods Eng n/a (n/a). doi:10.1002/nme.6359.
[25] Mesnil O, Recoquillay A, Druet T, Serey V, Hoang H, Imperiale A, et al. Experimental validation of transient spectral finite element simulation tools dedicated to guided wave based structural health monitoring. 2021. https://doi.org/10.1115/1.4050708.
[26] Gravenkamp H, Song C, Prager J. A numerical approach for the computation of dispersion relations for plate structures using the scaled boundary finite element method. J Sound Vib 2012;331(11):2543–57. https://doi.org/10.1016/j.jsv.2012.01.029.
[27] Mesnil O, Yan H, Ruzzene M, Paynabar K, Shi J. Fast wavenumber measurement for accurate and automatic location and quantification of defect in composite. Struct Health Monit 2016;15(2):223–34. https://doi.org/10.1177/1475921716636375.
[28] Bouvet C, Castanié B, Bizeul M, Barrau J-J. Low velocity impact modelling in laminate composite panels with discrete interface elements. Int J Solid Struct 2009;46(14):2809–21. https://doi.org/10.1016/j.ijsolstr.2009.03.010.
[29] J. Moll, C. Kexel, J. Kathol, C.-P. Fritzen, M. Moix-Bonet, C. Willberg, M. Rennoch, M. Koerdt, A. Herrmann, Guided waves for damage detection in complex composite structures: the influence of omega stringer and different reference damage size, Appl Sci 10 (9). doi:10.3390/app10093068.
[30] Leckey CA, Rogge MD, Miller CA, Hinders MK. Multiple-mode lamb wave scattering simulations using 3d elastodynamic finite integration technique. Ultrasonics 2012;52(2):193–207. https://doi.org/10.1016/j.ultras.2011.08.003.
[31] Segers J, Hedayatrasa S, Poelman G, Van Paepegem W, Kersemans M. Robust and baseline-free full-field defect detection in complex composite parts through weighted broadband energy mapping of mode-removed guided waves. Mech Syst Signal Process 2021;151:107360. https://doi.org/10.1016/j.ymssp.2020.107360.
[32] Kudela P, Radzienski M, Ostachowicz W. Impact induced damage assessment by means of lamb wave image processing. Mech Syst Signal Process 2018;102:23–36. https://doi.org/10.1016/j.ymssp.2017.09.020.
[33] Michaels JE, Dawson AJ, Michaels TE, Ruzzene M. Approaches to hybrid shm and nde of composite aerospace structures. In: Kundu T, editor. Health monitoring of structural and biological systems 2014, vol. 9064. SPIE: International Society for Optics and Photonics; 2014. p. 641–9. https://doi.org/10.1117/12.2045172.
[34] Info material for open-source strategy of BAM. https://github.com/BAMresearch/Open-Source-Software; 2020.